THE ATACAMA SURFACE SOLAR MAXIMUM

BY ROBERTO RONDANELLI, ALEJANDRA MOLINA, AND MARK FALVEY

By using a combination of satellite-derived datasets, we show that the location of Earth's surface solar radiation maximum is over the Atacama Desert.

Surface solar radiation is a major component of the surface heat budget. Diurnally and seasonally averaged over the entire Earth, 188 ± 7 W m^{-2} reach the surface to be either absorbed (~165 ± 6 W m^{-2}) or reflected back to the atmosphere (Trenberth et al. 2009; Stephens et al. 2012). Changes in the amount of solar radiation received at the surface are intrinsically tied to the total amount of precipitation through the surface heat balance (e.g., O'Gorman and Schneider 2008). Surface solar radiation is also a critical flux in the heat balance of both oceans and ice sheets (Reed 1977). Photosynthetic life forms owe their existence to the solar radiation in the visible part of the spectrum reaching the surface of the planet. On the other hand, the existence of bacterial life, for instance, can be limited by an excess of radiation in the ultraviolet (UV) part of the spectrum (Cockell et al. 2008). Moreover, exploiting surface solar radiation for energy production has become a major societal goal as the accessible fraction of the solar energy reaching Earth's surface is potentially several times the energy required for sustaining civilization.

For a given point at the surface of the planet, the amount of global or total horizontal solar radiation that can be measured by a broadband pyranometer [i.e., an instrument that measures the global solar irradiance, or the sum of direct plus diffuse radiation, typically over wavelengths between 0.2 and 3 mm (e.g., Iqbal 1983)] is dependent on ▶

View of the hills nearby Mount Montezuma in Atacama, the site of the most important solar station of the Smithsonian Astrophysical Observatory in the early twentieth century

the particular state of the sun (solar variability mostly at the 11-yr cycle), the present orbital configuration (obliquity, eccentricity, and precession of the equinoxes), the solar zenith angle, and most importantly the number of air molecules along the path (directly related to surface pressure), water vapor, ozone, clouds, and particles. Surface observations have been conducted over the years for all these quantities, but it is only recently, with the advent of radiometric instruments on satellites, that we have had a detailed distribution of all scatterers with sufficient global coverage and temporal resolution to allow the calculation of detailed maps of surface solar radiation. If we go back to the presatellite era, knowledge of the distribution of surface solar radiation was gathered by the combination of surface pyranometer observations plus the use of semiempirical formulas for the absorption and scattering of radiation [see, e.g., Kimball (1928) for an instance of an early semiempirical distribution of total solar radiation]. Information from a network of surface pyranometers (about 2,100 over the continents and 280 over the oceans) was used by Budyko (1974) to construct a semiempirical solar radiation map (see Fig. 1a). According to Budyko (1974, p. 151), the maximum solar radiation "is noted in northeastern Africa, due to the very slight cloudiness above this area." Budyko's surface solar distribution captures the main features of the latitudinal distribution of radiation—namely, the zonally symmetric distribution of solar radiation with relative minima over the midlatitude oceans and maxima over the subtropical regions of the planet. However, many interesting features of the global distribution of surface solar radiation are absent from Budyko's map, either because of the lack of data (most of the stations at that time were located over the Northern Hemisphere) or because of the coarse resolution of the map. In particular, the map misses entirely the location of the surface solar maximum in the Atacama. To Budyko's benefit, there is really no data over Atacama in his original map although solar radiation data in this region were collected during most of the twentieth century. However, a strong piece of anecdotal evidence that the Atacama was considered a solar optimum location as far back as the early twentieth century is the fact that the Smithsonian Astrophysical Observatory,

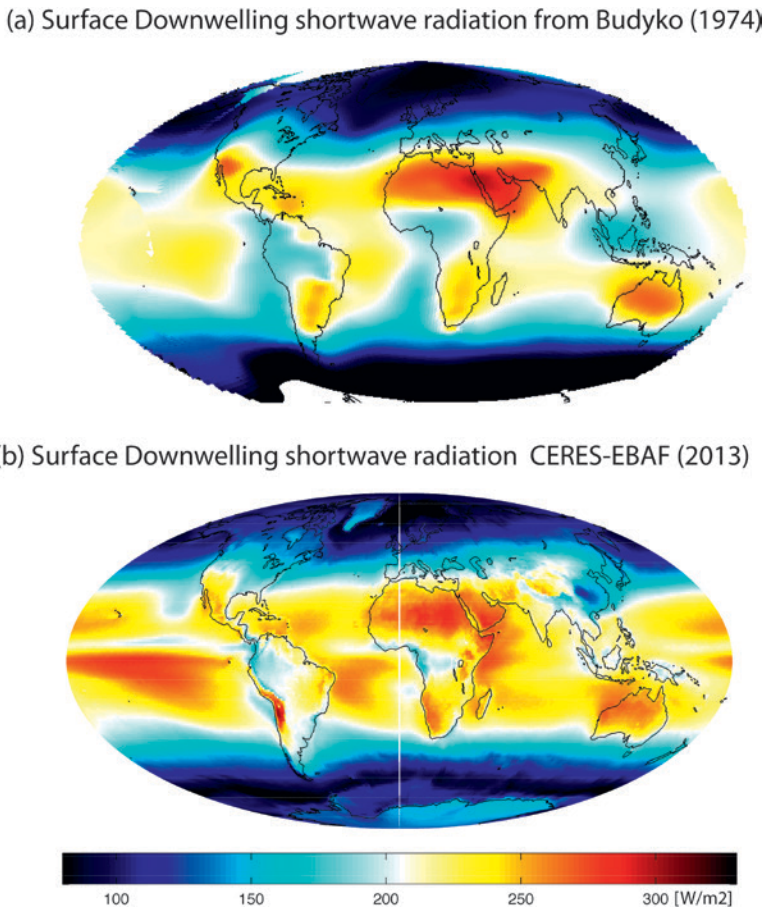

Fig. 1. Global distribution of surface solar radiation from (a) historical surface observations [adapted from Budyko (1974)] and (b) using state-of-the-art satellite information from CERES top-of-atmosphere radiances, cloud, aerosols, and water vapor distribution from a suite of A-Train measurements according to Kato et al. (2013). CERES–EBAF-derived field has a horizontal resolution of 1° × 1°.

AFFILIATIONS: Rondanelli—Department of Geophysics, University of Chile, and Center for Climate and Resilience Research, Santiago, Chile; Molina and Falvey—Department of Geophysics, University of Chile, Santiago, Chile
CORRESPONDING AUTHOR: Roberto Rondanelli, Department of Geophysics, University of Chile Santiago, Av. Blanco Encalada 2002, Santiago 6511228, Chile
E-mail: ronda@dgf.uchile.cl

The abstract for this article can be found in this issue, following the table of contents.
DOI:10.1175/BAMS-D-13-00175.1

In final form 17 September 2014

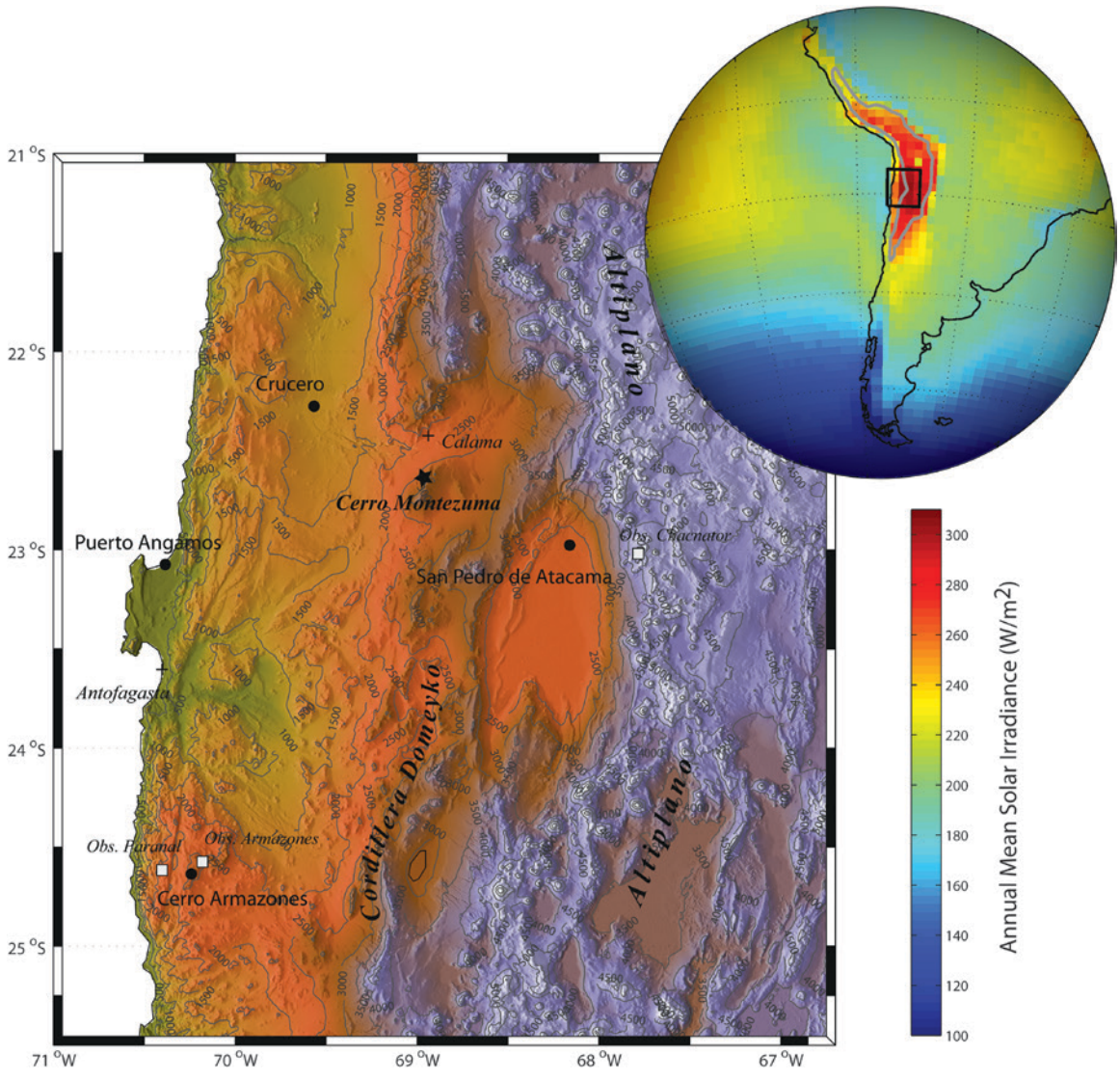

Fig. 2. Digital elevation map of the Atacama region showing some points of interest mentioned in the text. Current astronomical sites are marked with a white square. Surface solar radiation measurement stations are marked with black circles. The inset shows the distribution of surface solar radiation from the CERES–EBAF product.

lead initially by Samuel Langley, established a solar observatory in northern Chile, specifically at Calama in 1918 (Abbot 1918) (see Fig. 2). During the late nineteenth century and early twentieth century, the Smithsonian Astrophysical Observatory was largely concerned with the question of whether variations in the solar constant in the scales of months to years (that were believed to be significantly larger at that time) had a major bearing on weather and climate variations observed at the surface (e.g., Hoyt 1979 and references therein), and therefore the main purpose of the observatory established over northern Chile was to measure accurately changes in the solar constant with as little disturbances as possible from particles, clouds, or water vapor. Abbot (1918) briefly discusses the pilgrimage that finally led to the establishment of the Calama station [and later Mount Montezuma station (Fig. 2)] in the Atacama region and notes that the reasons for placing it in Atacama were not strictly scientific but also related to international politics and logistics. Calama–Mount Montezuma was the longest operating station of the Smithsonian solar program, and it recorded data almost continuously between 1918 and 1956 when the program ended without being able to establish conclusively a connection between solar variability and surface weather and climate.

The focus of this paper is to document the maximum of annual-mean surface solar irradiance (or global horizontal radiation) located over the coastal Atacama Desert between 22° and 25°S in the western

border of South America (see inset in Fig. 2). By using recent data mostly derived from the combination of satellite observations and radiative transfer models, we show the location and magnitude of this maximum in surface solar radiation. Abundant empirical evidence stresses the hyperaridity of the Atacama Desert (widely regarded as the world's driest area outside of the polar regions), while on the other hand, mostly anecdotal evidence points to Atacama as the region with the highest surface solar radiation. To our knowledge, there has been no systematic study to provide evidence for the claim of the highest surface radiation over some places in Atacama. Although it may seem frivolous or arbitrary to focus on the maximum solar radiation at the surface, this focus on the extreme solar radiation is interesting for several reasons. As it is usually the case for extremes, it requires the concurrence of several factors to explain it, which in passing allows us to discuss the factors that control the climatology of surface solar radiation in the planet. Also, and mostly because of the need of prospecting for new energy resources, different high-resolution tools (based on satellite data and empirical or analytical models of radiative transfer in the atmosphere) are emerging to provide a highly detailed distribution of solar radiation over the surface of the planet. Finally, the recognition of the solar maximum demonstrates the potential for an increase in the long-term observational capabilities over the Atacama region for the purpose of detecting trends in solar variations from the surface of the planet as well as for detecting changes in the amount of absorbers and scatterers related to natural and human causes.

GLOBAL DISTRIBUTION SURFACE SOLAR RADIATION, SCATTERERS, AND ABSORBERS. *Latitude and height variations.* In this section, we provide some necessary context to the claim of the Atacama surface solar maximum by discussing the main features of the global distribution of shortwave irradiance at the surface. Figure 1a shows the downwelling surface solar radiation, as inferred by Budyko (1974), mainly based on surface measurements. Figure 1b shows the downwelling surface solar radiation from the Clouds and the Earth's Radiant Energy System–Energy Balanced and Filled Surface Ed2.7 (CERES–EBAF-Surface_Ed2.7) product (Kato et al. 2013) averaged from March 2000 to February 2012. The CERES–EBAF product involves a suite of satellite-derived data from several different instruments [Atmospheric Infrared Sounder (AIRS), *Cloud–Aerosol Lidar and Infrared Pathfinder Satellite Observations (CALIPSO)* lidar data, *CloudSat* cloud radar, *Aqua* Moderate Resolution Imaging Spectroradiometer (MODIS) spectral radiances, and geostationary satellites radiances] combined with state-of-the-art radiative transfer models. Surface irradiances are calculated to be consistent with CERES-derived top-of-the-atmosphere radiances within the uncertainties in the cloud properties derived from satellite observations [see Kato et al. (2011, 2013) for more details].

According to the CERES–EBAF product, several regions of the planet show values of mean annual solar irradiance larger than about 250 W m^{-2}. The largest is perhaps the subtropical eastern Pacific region over the ocean that is a vast and remote area with the lowest fraction of cloud cover over the global oceans. Northeastern Africa (including the Sahara Desert) and the Arabian Peninsula are also shown as regions of high annual-mean global irradiance (higher than 280 W m^{-2}), associated with clear skies and low total column water vapor. On the other hand, minima in surface irradiance are located in the midlatitudes around 60° in each hemisphere with values lower than 100 W m^{-2}. These minima in surface solar irradiance are associated with maxima in the cloud fraction in the region of the Southern Hemisphere storm track that is collocated with minima in climatological surface pressure (Bromwich et al. 2012). Polar ice sheet regions in both hemispheres (including Greenland and Antarctica) show a much larger solar irradiance than adjacent oceans, especially over East Antarctica, where the steeper topography reduces the surface temperature and isolates the region from the influence of the ocean.

To clarify the relationship between orography, latitude, and atmospheric extinction, Fig. 3 shows the zonally averaged distribution of solar irradiance from different products and different assumptions on the composition of the atmospheric column above. Some of these calculations were performed using the radiative transfer parameterization of shortwave solar radiation developed by Chou and Suarez (2002). The red curve in Fig. 3 shows the distribution of mean extraterrestrial incoming solar radiation. Note that even at the poles horizontal incoming solar radiation remains substantial because of the tilt of Earth's axis. Incoming solar radiation decreases with latitude at a rate of about 2 W m^{-2} per degree of latitude in the tropics and about 4.5 W m^{-2} per degree of latitude in the extratropics. This distribution is first modified by the dry atmosphere through Rayleigh scattering and a smaller contribution by the absorption of molecular oxygen in both the UV and visible part of the spectrum (e.g., Liou 2002). The resulting "dry clear-sky" curve is shown by the black dotted curve

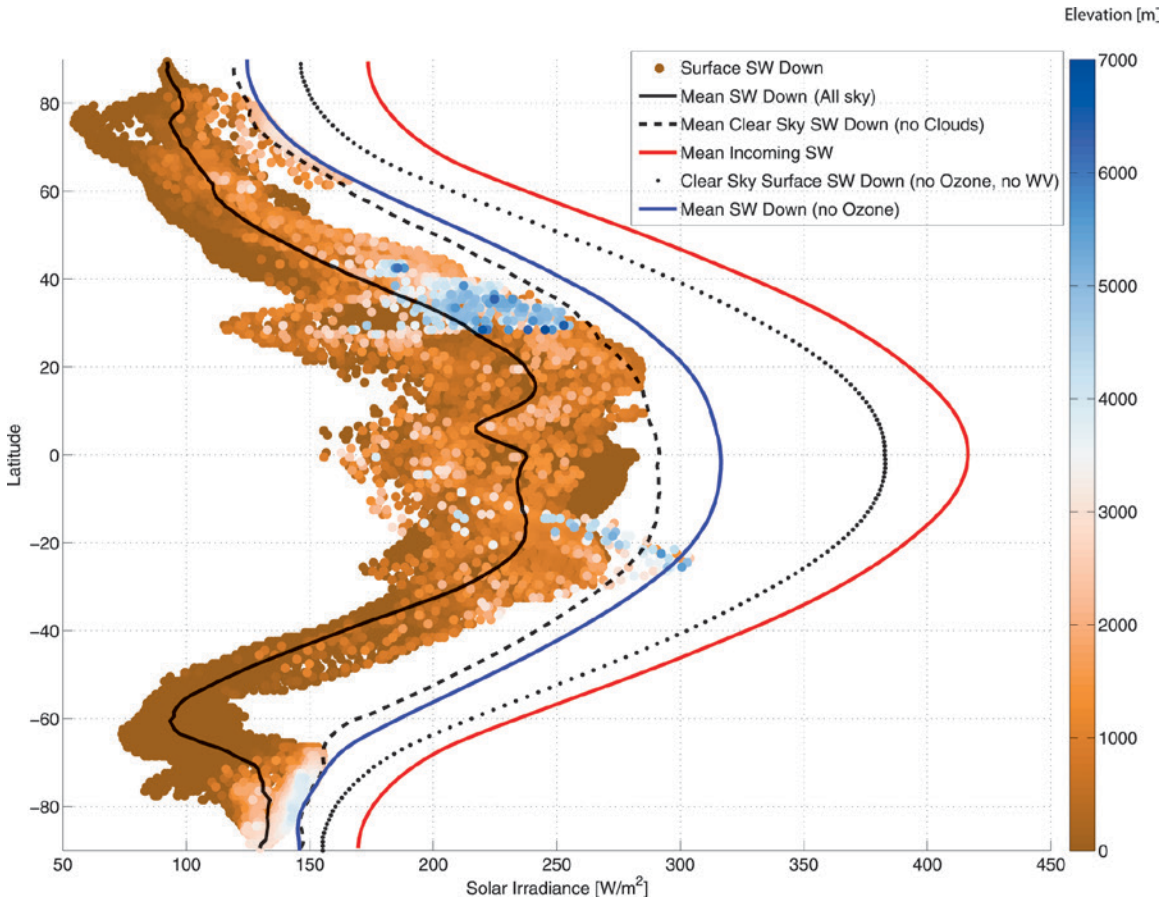

Fig. 3. Zonally averaged distribution of annual-mean surface solar irradiance (black), annual-mean clear-sky irradiance (dashed black), and annual-mean incoming solar irradiance at the top of the atmosphere (red) from the CERES–EBAF product. Also shown are the zonally averaged values of downwelling shortwave radiation calculated assuming a clear atmospheric column with no ozone and no water vapor (black dotted) as well as no ozone (blue) both using Chou and Suarez (2002) shortwave parameterization. The colored dots represent the value of the annual-mean solar irradiance for each grid point of the 1° × 1° CERES–EBAF Ed2.7 product (Kato et al. 2013). The points are color-labeled according to the elevation.

that represents the clear-sky radiation reaching the surface if no ozone or water vapor were present in the atmospheric column. The maximum reduction of radiation in the dry clear-sky situation occurs in the tropics (~30 W m^{-2}). A pronounced decrease in the radiation reaching the surface is obtained when climatological water vapor is added to the column (blue curve). The addition of water vapor further reduces the mean solar irradiance up to 20%, especially in the tropics where most of the water vapor is found. This reduction occurs as a sizeable amount of the near-infrared photons in the solar beam are absorbed mostly by water vapor and CO_2. Water vapor has therefore the effect of equalizing the distribution of surface radiation on the planet by means of the temperature dependence of the water vapor distribution. The black dashed curve shows the zonal-mean surface clear-sky irradiance from the CERES–EBAF product—that is, the situation when all absorbers and scatterers are present except for clouds. Given that ozone has a significant but small effect on the surface solar radiation, part of the difference between the blue and black dotted curve can be attributed to the direct radiative effect of aerosols, which can reach up to 30 W m^{-2} in regions like equatorial Africa and southeastern Asia [see, e.g., Fig. 9a in Kim and Ramanathan (2008)]. Finally, the solid black curve is the climatology of the zonally averaged surface solar radiation including the effects of all scatterers as derived from the CERES–EBAF product (Kato et al. 2013). Large departures of about 70 W m^{-2} from the clear-sky radiation (no clouds) represented by the black dashed curve occur in a relatively thin region of the tropics where the ITCZ is found and also in the

region of the westerlies in the Southern Hemisphere; these departures are explained by the persistent cloud coverage at these latitudes (reaching almost 100% in some regions; see Fig. 4a). Figure 3 illustrates that over the tropics the effect of water vapor alone in the extinction of surface solar radiation is of a similar magnitude as the combined effect of clouds and aerosols. Therefore, the role of water vapor can be anticipated as crucial to explain the location of the global solar maximum.

The color-coded dots in Fig. 3 represent each of the 1° × 1° grid boxes labeled according to the mean elevation of each individual grid points. From this dataset, it is evident that several grid points between 20° and 25°S and with an elevation ranging from 2000 to 6000 m above mean sea level depart significantly from the rest of the grid points at the same latitude and show values of the surface solar radiation that are even larger than the zonally averaged clear-sky radiation and the no-aerosol clear-sky curves. To be sure, these are also the highest elevations around the globe at this latitude. In contrast, the Himalayas region in the Northern Hemisphere, with even higher elevations and extension, does not show an equivalent departure from the mean latitudinal value of surface solar radiation. The relationship between topography and surface radiation is therefore not necessarily monotonic as is also evident when focusing on the region between 0° and 10°S where the highest surface solar radiation is found over the ocean in the clear region over the subtropical southern Pacific, rather than in the equatorial Andes.

The relationship between latitude and surface solar radiation is hardly monotonic either. As shown in Fig. 3, the zonal-mean surface solar radiation is greatest in the tropical regions with values of about 240 W m^{-2}. For a given latitude, variability in the surface radiation is higher than about 100 W m^{-2}. Regions of the planet, such as the eastern coast of China around 30°N, show small values of surface solar radiation (120–150 W m^{-2}) that would correspond to the mean at much higher latitudes (~50°N). Also striking is the distribution of surface solar radiation in the high-latitude regions of the Southern Hemisphere. Solar radiation shows a minimum near 60°S with higher values in the Antarctic Plateau. This produces an effective reversal of the mean latitudinal gradient of surface solar radiation in the region between 60°S and the South Pole as seen in Fig. 3.

By showing the global distribution of surface radiation in relation to the topography and latitude, we have attempted to show the critical role of the distribution of solar radiation scatterers and absorbers in setting the distribution of solar radiation. Downwelling shortwave irradiance is neither monotonic with latitude nor zonally symmetric and therefore the search for the global maximum in surface solar radiation is not just a case of finding the highest elevation at the lowest latitude. As noted above, the highest elevations in the equatorial region are in the Andes (~3500–5000 m), but they show some the lower values of surface solar radiation for that latitude. In the next section, we will briefly discuss the global distribution of these scatterers in relation to the surface solar radiation distribution; in particular, we will discuss the specific values of cloud fraction, water vapor, ozone, and aerosols found in the Atacama in comparison with the global distribution of these substances.

Global distribution of scatterers.

Cloud fraction. The global distribution of cloud fraction compiled from the MODIS instrument on board the *Terra* satellite from 2000 to 2009 is shown in Fig. 4a. Regions of relatively low cloud fraction (less than 20%) are concentrated in the subtropical continental regions of the planet around 20°S in northern Chile, South Africa, Australia, and around 20°N in the southwestern part of North America, the Arabic Peninsula, and North Africa where the lowest values appear to be found. These are all regions associated with subsidence over the continents in the subtropical belt away from both the tropical convergence zones and the midlatitude baroclinic storm tracks. To be sure, the oceans adjacent to the subtropical clear regions are usually associated with high cloud fractions because of the prevalence of stratocumulus in the western border of the continents, as is the case in the Atacama region, Namibia, California, and, to a lesser extent, Australia.

Precipitable water. Figure 4b shows the global distribution of precipitable water vapor as derived from MODIS on board the *Terra* satellite from 2000 to 2009. Precipitable water vapor distribution over the oceans is tightly constrained by sea surface temperature, given that most of the water vapor is found near the surface and global oceans have a rather homogeneous distribution of relative humidity of around 80%. The Clausius–Clapeyron relation therefore controls the amount of water vapor in the boundary layer, and one anticipates that warm oceanic regions show the highest values of precipitable water (most notably the Pacific warm pool; see Fig. 4b with more than 60 mm). On the other hand, low values of precipitable

water vapor (less than 5 mm) are found over the Tibetan Plateau, Atacama, Greenland, and Antarctica (all of them elevated regions). In section 3, we will discuss in more detail the processes that maintain the low precipitable water vapor over the Atacama region.

Ozone column. Although having a relatively modest role on the absorption of solar radiation for wavelengths longer than 0.34 mm, ozone molecular absorption is the dominant process for shorter wavelengths [see, e.g., calculations made by Noll et al. (2012) for Paranal Observatory mean conditions], and therefore changes in the ozone concentration also impact the total surface solar radiation. The total ozone global distribution is shown in Fig. 4c from a recent ozone climatology (TpO_3) based in ozonesondes and satellite data (Sofieva et al. 2014). The lowest values of the annual-mean ozone column are found over Antarctica (~250 DU, related to stratospheric ozone depletion) and over the tropical regions (~260 DU). Low total ozone concentrations over the Altiplano and Atacama regions are due primarily to the relatively low concentration of total ozone found in the tropics relative to midlatitudes. This general pattern is a consequence of the short photochemical lifetime of odd oxygen molecules in the tropical stratosphere of only hours, where ozone is mostly produced, relative to the photochemical lifetime of odd oxygen in the lower extratropical stratosphere that is on the order of months (Brasseur and Solomon 1986). Ozone produced in the tropical stratosphere is transported poleward and downward by the Brewer–Dobson circulation, where it accumulates in the lower stratosphere of high and midlatitudes because of the larger photochemical lifetime compared to the transport time scale (Dobson 1956; Fioletov 2008). In addition, the relatively high elevation of the Atacama region contributes to a further reduction in the total ozone column [~10 DU over the Altiplano with respect to the sea level (Kirchhoff and Guarnieri 2002)]. Related to the main theme of this study and because of the combination of factors so far discussed,

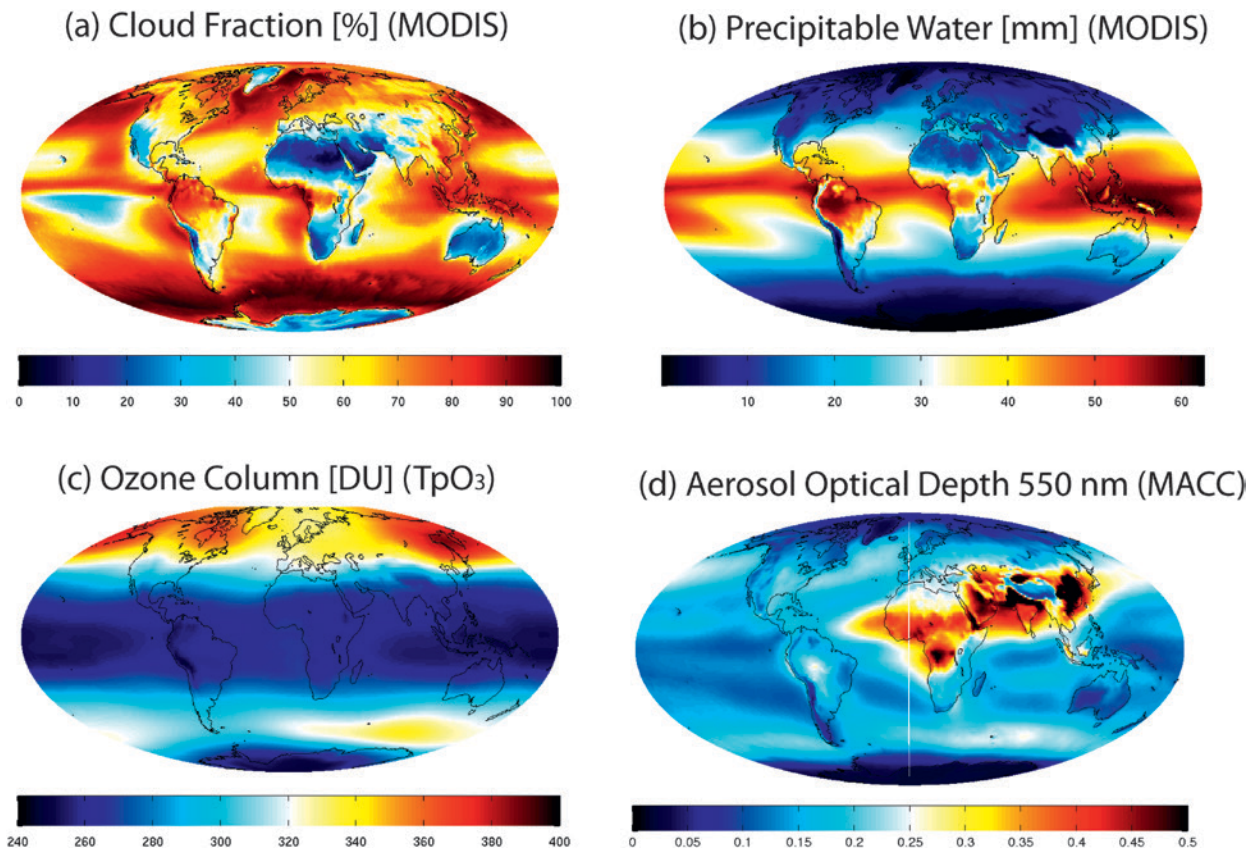

Fig. 4. Climatology of the global distribution of solar absorbers and scatterers, according to several global products. (a) Cloud coverage fraction (%) from MODIS-*Terra* from years 2000 to 2009. (b) Precipitable water (mm) from MODIS-*Terra* from years 2000 to 2009. (c) Integrated ozone column in Dobson units (DU) from the TpO_3 climatology (based on data from 1980 to 2006) (Sofieva et al. 2014). (d) Aerosol optical thickness at 550 nm from the MACC reanalysis from years 2003 to 2010. (Bellouin et al. 2013).

measurements of UV radiation at Chajnantor and Paranal (see Fig. 2) made by Cordero et al. (2014) and at Licancabur volcano (22.5°S, 67.53°W; 5,917 m) reported by Cabrol et al. (2014) show the highest values ever recorded of the UV index at Earth's surface.

Aerosol optical thickness. Aerosol optical depth (AOD) at 550 nm is shown in Fig. 4 from the Monitoring Atmospheric Composition and Climate (MACC) gas and aerosol reanalysis products (Bellouin et al. 2013). Again, the Atacama appears as a region with little influence from the major regional aerosol sources. The most important source of aerosols in South America is biomass burning over the Amazon region. The Atacama region appears to be mostly isolated from the influence of biomass burning aerosols because of the barrier provided by the high Andes. One may hypothesize that low aerosol values found over the Atacama region might also be related to the Andes acting as a "wet trap" for the westward transport of aerosols from the Amazon region. In fact, when the circulation is conducive to transport to the Altiplano from the low lands on the eastern side of the Andes, it is also when precipitation is favored (Garreaud and Aceituno 2001) and therefore particles are likely to be further removed by wet deposition. One should mention, however, that biomass burning is concentrated in September, October, and November and is out of phase with the Altiplano and Amazon rainy seasons. The simulated distribution of aerosols from biomass burning including processes such as the wet removal shows almost no influence of biomass burning in particle concentration or AOD below about 20°S on the western slope of the Andes (Freitas et al. 2005).

The MACC reanalysis product shows AOD at 550 nm between 0.05 and 0.1 over the Atacama region—some of the lowest values outside of polar regions. Spectrophotometric estimations made at the Cerro Paranal Astronomical Observatory during 2008/09 confirm low values for this particular site of about 0.03 for AOD at 550 nm (Patat et al. 2011). These are in striking contrast with the relatively high mean values of AOD found in the Sahara and especially the sub-Saharan region (between 0.2 and 0.4) associated primarily with mineral dust but also with anthropogenic sources (Bellouin et al. 2013).

ATACAMA SOLAR CLIMATE. The Atacama region is well known by its hyperaridity—that is, the very low ratio between surface precipitation and potential evaporation. Many places in the Atacama barely receive any precipitation for periods that can last several decades [Antofagasta (23.65°S at sea level; see Fig. 2) has a climatological annual mean of 3.2 mm, whereas Calama (22.46°S; 2,300 m MSL) has an annual mean of 4.2 mm (Houston 2006)]. To the extent that the absence of water vapor and clouds is common to both hyperaridity and extreme surface solar radiation, a discussion on the hyperaridity of the Atacama Desert is also relevant to our discussion of the solar climate of the region.

Atacama hyperaridity. The hyperaridity of the Atacama has been connected to the concurrence of several factors:

1) The location of the Atacama region over the subtropical belt under the influence of the subsiding air of the southeastern Pacific subtropical anticyclone in the descending branch of Hadley circulation. This large-scale subsidence has been shown to be increased further over the Atacama Desert and adjacent southeastern Pacific by the response to the latent heat released by tropical convection over the continent. According to Rodwell and Hoskins (2001), this additional subsidence results from the interaction between a Rossby wave response to tropical heating over South America and the midlatitude westerlies.
2) The associated southerly flow in low levels along the Atacama coast induces cooling of the adjacent ocean through mixing, upwelling, and advection of cold waters. The anomalously "cool for the latitude" sea surface temperature offshore strengthens the static stability given that the temperature in the tropical free troposphere is controlled nonlocally by the convective heating in the whole tropical atmosphere (e.g., Sobel 2002).
3) This increased stability and subsidence is associated with the formation of a persistent deck of stratocumulus that extends along the coast from 70° to about 120°W (e.g., Bretherton et al. 2010; Wood 2012) with mean frequencies of about 60%–70% throughout the year (see Fig. 4a). The dryness of the free troposphere above induces a strong radiative cooling at the top of the stratocumulus layer that furthers the subsidence inversion and reinforces the stable boundary layer below. The mean altitude of the base of the subsidence inversion at around 22°S, which marks the top of the cloud, is approximately 1,000 m (Garreaud et al. 2008). Therefore, the stratocumulus deck frequently intercepts the coastal range. The mutual interaction between the stratocumulus layer and topography constrains the humidity

of the boundary layer to the low coastal region (which in places is only a few kilometers inland). However, there appears to be episodic mixing of boundary layer air, especially during summer when the height of the base of the inversion layer surpasses the mean height of the topography (Rutllant et al. 2003; Falvey and Garreaud 2005). This results in the climatological minimum of specific humidity in the free troposphere occurring over the ocean at the latitude of the Atacama. Further evidence for the episodic mixing between high humidity air in the cloud-topped boundary layer and dry air from large-scale subsidence has been provided by Galewsky et al. (2011) to explain the range of water vapor isotopic composition observed at Chajnantor (23°S, ~5,000 m; see Fig. 2).

4) Heating of the arid slope of the Andes over the Atacama results in additional afternoon subsidence over the coastal region that is several times larger than the one induced by the anticyclone itself (Rutllant et al. 2003). The additional subsidence above the subsidence inversion layer in the coastal and central depression region of the Atacama is driven by the strong horizontal contrast between the heating of the slopes during daytime and the relatively cool air above the stratocumulus region and the associated zonal divergence of the upslope flow.

5) Finally, and more controversially, is the role that the Andes itself plays as a mechanical barrier for the transport of water vapor from the Amazon and Atlantic regions [a good summary of the controversy is provided in Garreaud et al. (2010)]. Essentially, it is postulated that at the latitudes of the Atacama Desert (especially between 18° and 22°S where the Andes can reach a mean altitude of about 5,000 m), the orography forces a southward transport of water vapor from the Amazon through the Pampas low-level jet on the eastern side of the Andes and acts as well as a rain shadow for precipitation (Houston and Hartley 2003; Rech et al. 2006). However, numerical experiments carried out by Garreaud et al. (2010) using the Planet Simulator (PLASIM) model (Fraedrich et al. 2005) show that removing the Andes barrier does not have a significant impact

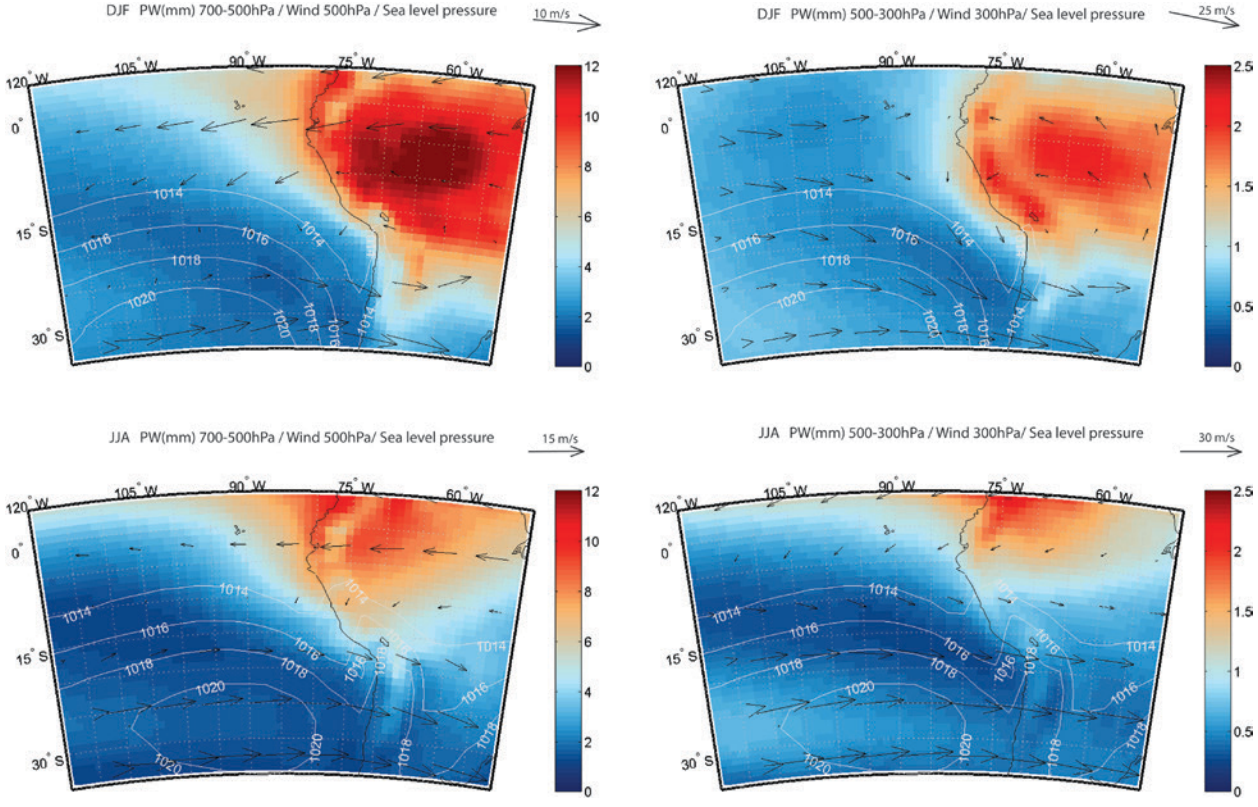

Fig. 5. Climatology (1988–2010) of precipitable water in the free troposphere between the levels of 700 and 500 hPa for (a) DJF and (c) JJA and for the level between 500 and 300 hPa for (b) DJF and (d) JJA together with wind vectors at the corresponding upper level of each layer from reanalysis as well as climatological surface pressure (hPa; white contours) (Kalnay et al. 1996). Water vapor data are from the NVAP-M product (Vonder Haar et al. 2012).

on the amount of precipitation in the Atacama and therefore does not change the hyperarid character of the desert in their reduced topography simulations. Rather, the effect is a drying of the present-day eastern slope of the Andes at that latitude, which would now increase the spatial influence of the subsidence induced by the subtropical anticyclone. Inspecting the Garreaud et al. (2010) simulations with reduced topography (even with the Andes having 10% the present height), no significant increase in water vapor is seen in the free troposphere above 800 hPa. So, for this particular model, the maintenance of the hyperarid conditions in the Atacama occurs under no increase in water vapor either; therefore, the effect of removing the Andes in the solar transmission is robustly small (except of course for the change in elevation). The fact that even small increases in the absolute values of water vapor can change this result (because of the already dry atmosphere) warrant keeping in mind the limitations of a model such as PLASIM in simulating accurately the transport of water vapor over Atacama. Calculations made with the CLIRAD-SW parameterization (Chou and Suarez 2002) using a climatological profile representative of the region show that changing the precipitable water vapor (PW) from 2 to 6 mm over Atacama reduces the surface solar radiation by about 3%.

Regional distribution of free-tropospheric water vapor. To illustrate the relation between the moisture sources on the eastern slope of the Andes and potential transport of moisture over the Andes into the Pacific, we show the climatological distribution of PW in free-tropospheric layers over the interest region in South America (Fig. 5). Precipitable water is shown for pressure layers between 700 and 500 hPa and 500 and 300 hPa according to the NASA Water Vapor Project-Making Earth Science Data Records for Research Environments (MEaSUREs) (NVAP-M) product (Vonder Haar et al. 2012). For the purpose of the solar climate of the region, the PW distribution is relevant not only because of the role of water vapor itself in the decrease of surface radiation, but also because upper-level water vapor serves as a proxy for the upper-level cloud distribution that further modifies the surface radiation field.

As can be seen in Figs. 5a and 5b, the zonal gradient of PW along the coast at the Atacama latitudes is reversed from what is observed by looking at the conventional value of PW integrated from the surface in Fig. 4b; that is, the minimum PW in the free troposphere is located over the ocean closer to the coast during December–February (DJF) and farther off the coast during June–August (JJA) following the north–south drift of the eastern Pacific subtropical anticyclone (1–2 mm in the 700–500-hPa layer and less than 1 mm in the 500–300-hPa layer). The minima in free-tropospheric PW are located on the equatorward side of the surface anticyclone. The distribution of PW over tropical and subtropical South America is dominated by the large maximum over the Amazon, especially in the 700–500-hPa layer during DJF (~12 mm). The 500–300-hPa layer also shows a distinct PW signature over the Amazon and more clearly over the Altiplano (~2 mm) during DJF because of the monsoonal convective activity. It is evident from Fig. 5 that the circulation established by the Bolivian high plays a critical role in setting the northwest–southeast elongated shape of the humidity distribution. North of about 20°–22°S along the coast and where the upper-level circulation has an easterly component, free-tropospheric values of water vapor are relatively high compared to the remote oceanic regions at the same latitude, likely the result of the advection of water vapor from the convective activity. This is particularly evident along 10°S in the layer between 500 and 300 hPa, where a seasonal reversal between easterly and westerly winds is associated with the formation of a strip of about 500-km width that follows the shape of the coast with relatively large values of PW over the ocean during the austral summer. This is likely the result of episodic transport of water vapor (and upper-level clouds) detrained from the outflow of the Altiplano convective activity. This is evident from looking at geostationary satellite imagery of individual cases (e.g., Garreaud 2011) and also consistent with the increase over the adjacent ocean of PW between wet and dry episodes during the 2002/03 summer (Falvey and Garreaud 2005). As shown in Fig. 5b, the northeasterly flow south of about 10°S over the ocean brings moist air north of 20°S and dry air south of 20°S. This will become important to explain the precise location of the surface maximum. During wintertime the role of the subtropical jet (along 30°S; see Fig. 5d) in advecting low PW air from the ocean humidity minimum is particularly evident. Mostly during wintertime, synoptic-scale transport of very low humidity air from high latitudes and upper levels in the troposphere, and presumably the stratosphere, has been documented (Kerber et al. 2014), which further contributes to the extreme dryness found over the Atacama, especially during winter.

Regional distribution of radiation from a semiempirical model and surface observations. To show in more detail the location and magnitude of the surface solar maximum, we make use of a high-resolution semiempirical simple model of surface solar radiation developed by Molina (2012). To calculate the clear-sky radiation, the CLIRAD-SW radiative transfer parameterization (Chou and Suarez 2002) is used. Atmospheric profiles to feed the radiative transfer calculations have been obtained from the National Centers for Environmental Prediction–National Center for Atmospheric Research (NCEP–NCAR) reanalysis (temperature, specific humidity, and pressure; Kalnay et al. 1996) and aerosol optical thickness was obtained from the MACC reanalysis (Bellouin et al. 2013). A 1-km-horizontal-resolution topography has also been incorporated into the model. From *Geostationary Operational Environmental Satellite East (GOES-East)* imager scans in the visible band, a reflectivity coefficient is obtained for each pixel for the cloudy sky. To incorporate the effect of cloudiness into the surface solar radiation, an empirical model has been developed and validated that relates the clear-sky radiation and cloud reflectivity to ground-based global horizontal solar radiation measurements in places that have a relatively high frequency of clouds. Clouds are distinguished from snow using the MODIS snow dataset, version 5 (Riggs et al. 2006). In this simple model, the effect of surface albedo in modifying the downwelling surface radiation has been neglected. Using this methodology, the global horizontal radiation at 1-km horizontal resolution has been calculated for most of the Chilean continental territory, between 19° and 45°S, for all times in which visible images from GOES were available (Molina 2012). It has been found that the mean error in the annual-mean surface solar radiation is about 5% by comparing model results with independent surface measurements.

Figure 6a shows the resulting annual-mean surface solar radiation for a region that covers most of the

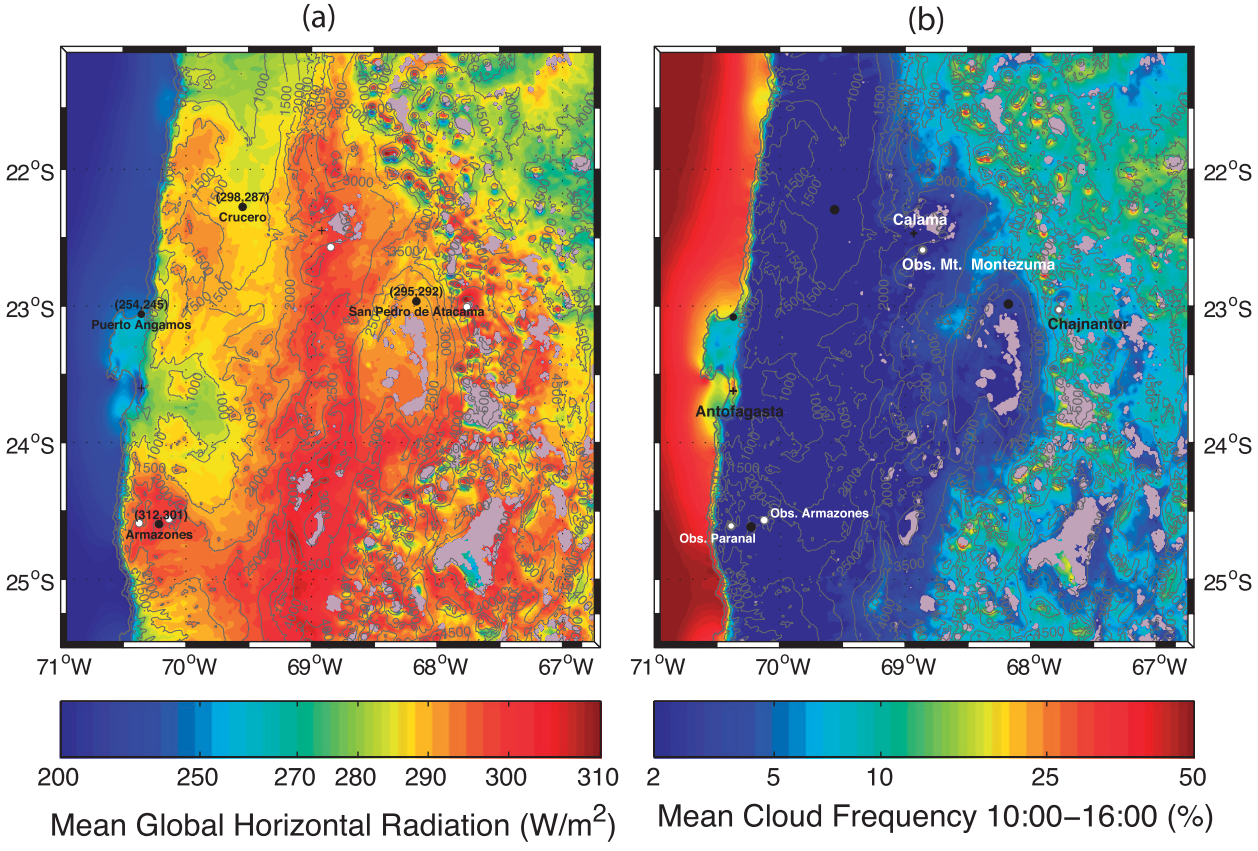

Fig. 6. (a) The global horizontal surface radiation calculated from a semiempirical model (Molina 2012). The location of surface observations is shown with black dots. The numbers between parentheses correspond to the observed and modeled mean surface radiation in the format (observation, model). Other sites of interest are shown as white dots. (b) Mean cloud fraction between 1000 and 1600 local time derived from geostationary satellite data in the visible channel. Both panels correspond to the mean climatological value from 2004 to 2012. Gray areas are regions in which the high albedo of the surface, owing to snow cover or salt pans, precludes the identification of clouds from the model algorithm.

Atacama Desert. Gray regions in the figure show pixels in which no satisfactory discrimination between clouds and the surface was reached (because of snow cover or salt pans). The figure also shows the observed values of surface solar radiation for four stations that were not used in the calibration of the empirical model and that are known to have high-quality maintenance procedures. Surface measurements are from CMP11 pyranometers manufactured by Kipp and Zonnen mounted at 2 m over the surface and cleaned on, at least, a monthly basis. The stations have a series of 3–4.5 years of data in the period 2009–13. A large gradient is seen in the surface solar radiation across the coast and into the coastal range with increases of 70–80 W m^{-2} over the distance of a few kilometers across the coast. As seen in Fig. 6b, this is the signature of the prevalent stratocumulus cloud cover over the coastal region in the first 1,000 m or so above sea level. Farther inland, radiation increases mostly with height at a rate of about 10 W m^{-2} km^{-1}. The absolute maximum, according to the semiempirical model, is found in the region between 24° and 25°S along 69°W, over what is known as the Domeyko Cordillera (see Fig. 2). The Domeyko Cordillera is a mountain range that spans from about 22° to 26°S in a mostly north–south orientation with elevations ranging from 3,500 to 5,000 m. The origin of this range is the tectonic uplift during the Eocene, mostly before 30 Ma (Strecker et al. 2007), and is the locus of some of the most important copper deposits on the planet.

By looking at the mean cloud fraction distribution one finds that the High Andes are associated with relatively high cloud fractions related to episodic summertime convection (from about 5% to 25%), a manifestation of the South American monsoon. The Domeyko Cordillera is severed from the moisture source from the Altiplano by the Andes. On the other hand, the relatively southern location of the range puts it well into the westerly circulation from the dry ocean both in summer and winter, as well as being equatorward of most of the wintertime midlatitude weather systems that only rarely reach north of 25°S. Other places in the region also show values of radiation that are likely higher than any other place on the surface of the planet. Even with higher cloud cover than the Domeyko Cordillera (10% vs 4%), the surface solar radiation region in the Altiplano between 67° and 68°W and at an elevation of 4,500 m is shown having more than 300 W m^{-2}. Given the relatively large interannual and seasonal variability over the Altiplano region, one may expect the global maximum to shift to this region during individual years. Given the error involved in the semiempirical model of about 15 W m^{-2}, the precise magnitude and location of the maximum remains to be determined. As a matter of fact, the Armazones station (24.6°S; 2,580 m), as shown in Fig. 6a, has recorded a mean of 312 W m^{-2} from years 2011 to 2013, higher than the maximum value from the semiempirical model of 308 W m^{-2} at the Domeyko Cordillera at an elevation of about 3,500 m.

SUMMARY. We have presented a descriptive analysis showing a suite of different global products that combine information from models and satellites to provide the global distribution of surface total solar radiation as well as the distribution of the main substances that explain the atmospheric extinction of solar radiation reaching the surface. Latitude, elevation, cloud fraction, water vapor, and aerosols have a first-order influence on the distribution of surface solar radiation over the planet, and no single factor explains the combined distribution. The most likely location of the total solar radiation over the surface of the planet is on the pre-Andean Domeyko Cordillera, a mountain range with elevations between 3,500 and 5,000 m. The regional climate of the Atacama is such that extremely low values of water vapor, cloud cover, ozone, and aerosols concur in this region. The atmospheric transparency in the visible and infrared provided by these conditions, together with a relatively high elevation and low latitude, conspire to produce a region where mean total radiation values exceed 300 W m^{-2}. According to a semiempirical model for surface solar radiation that takes into account extinction by gases, clouds, aerosols, and the effect of topography, the maximum is about 310 ± 15 W m^{-2}, although for individual years, especially those with dry summertime Altiplano conditions, the solar maximum should be located in the Altiplano region near to the Chajnantor Plateau. The delicate combination of elements that concurs in the Atacama region still justifies the increase in observational capabilities of solar radiation and atmospheric composition as it was first devised and executed by the pioneers of solar research in Mount Montezuma in the early twentieth century.

ACKNOWLEDGMENTS. The authors appreciate suggestions and comments provided by José (Pepe) Rutllant and two anonymous reviewers. Alejandra Molina and Mark Falvey acknowledge support from the Chilean Ministry of Energy. Roberto Rondanelli acknowledges support from the Center for Climate and Resilience Research, CONICYT/FONDAP/15110009, and from FONDECYT (Chile) Grant 1120040. The CERES–EBAF-Surface_Ed2.7 product data were obtained from the Langley Research Center CERES ordering tool at http://ceres.larc.nasa.gov/.

REFERENCES

Abbot, C. G., 1918: The Smithsonian 'Solar Constant' Expedition to Calama, Chile. *Proc. Natl. Acad. Sci. USA,* **4,** 313–316, doi:10.1073/pnas.4.10.313.

Bellouin, N., J. Quaas, J.-J. Morcrette, and O. Boucher, 2013: Estimates of aerosol radiative forcing from the MACC re-analysis. *Atmos. Chem. Phys.,* **13,** 2045–2062, doi:10.5194/acp-13-2045-2013.

Brasseur, G., and S. Solomon, 1986: *Aeronomy of the Middle Atmosphere: Chemistry and Physics of the Stratosphere and Mesosphere.* 2nd ed. Reidel, 452 pp.

Bretherton, C., R. Wood, R. George, D. Leon, G. Allen, and X. Zheng, 2010: Southeast Pacific stratocumulus clouds, precipitation and boundary layer structure sampled along 20 s during VOCALS-REx. *Atmos. Chem. Phys.,* **10,** 10 639–10 654, doi:10.5194/acp-10-10639-2010.

Bromwich, D. H., and Coauthors, 2012: Tropospheric clouds in Antarctica. *Rev. Geophys.,* **50,** RG1004, doi:10.1029/2011RG000363.

Budyko, M. I., 1974: *Climate and Life.* International Geophysics Series, Vol. 18, D. H. Miller, Ed., Academic Press, 508 pp.

Cabrol, N. A., U. Feister, D. P. Häder, H. Piazena, E. A. Grin, and A. Klein, 2014: Record solar UV irradiance in the tropical Andes. *Front. Environ. Sci. Environ. Toxicol.,* **2,** doi:10.3389/fenvs.2014.00019.

Chou, M., and M. Suarez, 2002: A solar radiation parameterization for atmospheric studies. NASA Tech. Rep. NASA/TM-1999-10460, 42 pp.

Cockell, C. S., C. P. McKay, K. Warren-Rhodes, and G. Horneck, 2008: Ultraviolet radiation-induced limitation to epilithic microbial growth in arid deserts—Dosimetric experiments in the hyperarid core of the Atacama Desert. *J. Photochem. Photobiol.,* **90B,** 79–87, doi:10.1016/j.jphotobiol.2007.11.009.

Cordero, R. R., G. Seckmeyer, A. Damiani, S. Riechelmann, J. Rayas, F. Labbe, and D. Laroze, 2014: The world's highest levels of surface UV. *Photochem. Photobiol. Sci.,* **13,** 70–81, doi:10.1039/c3pp50221j.

Dobson, G., 1956: Origin and distribution of the polyatomic molecules in the atmosphere. *Proc. Roy. Soc. London.,* **A236,** 187–193. [Available online at www.jstor.org/stable/100027.]

Falvey, M., and R. D. Garreaud, 2005: Moisture variability over the South American Altiplano during the South American Low Level Jet Experiment (SALLJEX) observing season. *J. Geophys. Res.,* **110,** D22105, doi:10.1029/2005JD006152.

Fioletov, V., 2008: Ozone climatology, trends, and substances that control ozone. *Atmos.–Ocean,* **46,** 39–67, doi:10.3137/ao.460103.

Fraedrich, K., H. Jansen, E. Kirk, U. Luksch, and F. Lunkeit, 2005: The planet simulator: Towards a user friendly model. *Meteor. Z.,* **14,** 299–304, doi:10.1127/0941-2948/2005/0043.

Freitas, S. R., and Coauthors, 2005: Monitoring the transport of biomass burning emissions in South America. *Environ. Fluid Mech.,* **5,** 135–167, doi:10.1007/s10652-005-0243-7.

Galewsky, J., C. Rella, Z. Sharp, K. Samuels, and D. Ward, 2011: Surface measurements of upper tropospheric water vapor isotopic composition on the Chajnantor Plateau, Chile. *Geophys. Res. Lett.,* **38,** L17803, doi:10.1029/2011GL048557.

Garreaud, R. D., 2011: The climate of northern Chile: Mean state, variability and trends. *Rev. Mex. Astron. Astrofis.,* **41,** 5–11.

——, and P. Aceituno, 2001: Interannual rainfall variability over the South American Altiplano. *J. Climate,* **14,** 2779–2789, doi:10.1175/1520-0442(2001)014<2779:IRVOTS>2.0.CO;2.

——, J. Barichivich, D. Christie, and A. Maldonado, 2008: Interannual variability of the coastal fog at Fray Jorge relict forests in semiarid Chile. *J. Geophys. Res.,* **113,** G04011, doi:10.1029/2008JG000709.

——, A. Molina, and M. Farias, 2010: Andean uplift, ocean cooling and Atacama hyperaridity: A climate modeling perspective. *Earth Planet. Sci. Lett.,* **292,** 39–50, doi:10.1016/j.epsl.2010.01.017.

Houston, J., 2006: Variability of precipitation in the Atacama Desert: Its causes and hydrological impact. *Int. J. Climatol.,* **26,** 2181–2198, doi:10.1002/joc.1359.

——, and A. J. Hartley, 2003: The central Andean west-slope rainshadow and its potential contribution to the origin of hyper-aridity in the Atacama Desert. *Int. J. Climatol.,* **23,** 1453–1464, doi:10.1002/joc.938.

Hoyt, D. V., 1979: The Smithsonian Astrophysical Observatory solar constant program. *Rev. Geophys.,* **17,** 427–458, doi:10.1029/RG017i003p00427.

Iqbal, M., 1983: *An Introduction to Solar Radiation.* Academic Press, 390 pp.

Kalnay, E., and Coauthors, 1996: The NCEP/NCAR 40-Year Reanalysis Project. *Bull. Amer. Meteor. Soc.,* **77,** 437–471, doi:10.1175/1520-0477(1996)077<0437:TNYRP>2.0.CO;2.

Kato, S., and Coauthors, 2011: Improvements of top-of-atmosphere and surface irradiance computations with *CALIPSO*-, *CloudSat*-, and MODIS-derived cloud and aerosol properties. *J. Geophys. Res.,* **116,** D19209, doi:10.1029/2011JD016050.

——, N. G. Loeb, F. G. Rose, D. R. Doelling, D. A. Rutan, T. E. Caldwell, L. Yu, and R. A. Weller, 2013: Surface irradiances consistent with CERES-derived

top-of-atmosphere shortwave and longwave irradiances. *J. Climate,* **26,** 2719–2740, doi:10.1175/JCLI-D-12-00436.1.

Kerber, F., and Coauthors, 2014: An episode of extremely low precipitable water vapour over Paranal Observatory. *Mon. Not. Roy. Astron. Soc.,* **439,** 247–255, doi:10.1093/mnras/stt2404.

Kim, D., and V. Ramanathan, 2008: Solar radiation budget and radiative forcing due to aerosols and clouds. *J. Geophys. Res.,* **113,** D02203, doi:10.1029/2007JD008434.

Kimball, H. H., 1928: Amount of solar radiation that reaches the surface of the earth on the land and on the sea, and methods by which it is measured. *Mon. Wea. Rev.,* **56,** 393–398, doi:10.1175/1520-0493(1928)56<393:AOSRTR>2.0.CO;2.

Kirchhoff, V., and F. Guarnieri, 2002: Missing ozone at high altitude: Comparison of in situ and satellite data. *J. Geophys. Res.,* **107,** doi:10.1029/2001JD000810.

Liou, K.-N., 2002: *An Introduction to Atmospheric Radiation.* International Geophysics Series, Vol. 84, Academic Press, 583 pp.

Molina, A., 2012: A semi-empirical model for surface solar radiation in Chile (in Spanish). M.S. thesis, Department of Geophysics, University of Chile, 32 pp.

Noll, S., W. Kausch, M. Barden, A. Jones, C. Szyszka, S. Kimeswenger, and J. Vinther, 2012: An atmospheric radiation model for Cerro Paranal. I. The optical spectral range. *Astron. Astrophys.,* **543,** A92, doi:10.1051/0004-6361/201219040.

O'Gorman, P. A., and T. Schneider, 2008: The hydrological cycle over a wide range of climates simulated with an idealized GCM. *J. Climate,* **21,** 3815–3832, doi:10.1175/2007JCLI2065.1.

Patat, F., and Coauthors, 2011: Optical atmospheric extinction over Cerro Paranal. *Astron. Astrophys.,* **527,** A91, doi:10.1051/0004-6361/201015537.

Rech, J. A., B. S. Currie, G. Michalski, and A. M. Cowan, 2006: Neogene climate change and uplift in the Atacama Desert, Chile. *Geology,* **34,** 761–764, doi:10.1130/G22444.1.

Reed, R., 1977: On estimating insolation over the ocean. *J. Phys. Oceanogr.,* **7,** 482–485, doi:10.1175/1520-0485(1977)007<0482:OEIOTO>2.0.CO;2.

Riggs, G., D. Hall, and V. Salomonson, 2006: MODIS snow products user guide to collection 5. National Snow and Ice Data Center, Boulder, CO, digital media. [Available online at http://modis-snow-ice.gsfc.nasa.gov/uploads/sug_c5.pdf.]

Rodwell, M., and B. Hoskins, 2001: Subtropical anticyclones and summer monsoons. *J. Climate,* **14,** 3192–3211, doi:10.1175/1520-0442(2001)014<3192:SAASM>2.0.CO;2.

Rutllant, J. A., H. Fuenzalida, and P. Aceituno, 2003: Climate dynamics along the arid northern coast of Chile: The 1997–1998 Dinámica del Clima de la Región de Antofagasta (DICLIMA) experiment. *J. Geophys. Res.,* **108,** 4538, doi:10.1029/2002JD003357.

Sobel, A. H., 2002: Water vapor as an active scalar in tropical atmospheric dynamics. *Chaos,* **12,** 451–459, doi:10.1063/1.1480795.

Sofieva, V., J. Tamminen, E. Kyrölä, T. Mielonen, P. Veefkind, B. Hassler, and G. Bodeker, 2014: A novel tropopause-related climatology of ozone profiles. *Atmos. Chem. Phys.,* **14,** 283–299, doi:10.5194/acp-14-283-2014.

Stephens, G. L., and Coauthors, 2012: An update on Earth's energy balance in light of the latest global observations. *Nat. Geosci.,* **5,** 691–696, doi:10.1038/ngeo1580.

Strecker, M., R. Alonso, B. Bookhagen, B. Carrapa, G. Hilley, E. Sobel, and M. Trauth, 2007: Tectonics and climate of the southern central Andes. *Annu. Rev. Earth Planet. Sci.,* **35,** 747–787, doi:10.1146/annurev.earth.35.031306.140158.

Trenberth, K. E., J. T. Fasullo, and J. Kiehl, 2009: Earth's global energy budget. *Bull. Amer. Meteor. Soc.,* **90,** 311–323, doi:10.1175/2008BAMS2634.1.

Vonder Haar, T. H., J. L. Bytheway, and J. M. Forsythe, 2012: Weather and climate analyses using improved global water vapor observations. *Geophys. Res. Lett.,* **39,** L15802, doi:10.1029/2012GL052094.

Wood, R., 2012: Stratocumulus clouds. *Mon. Wea. Rev.,* **140,** 2373–2423, doi:10.1175/MWR-D-11-00121.1.